Numerical Design of CoNi-Base Superalloys With Improved Casting Structure

BENJAMIN WAHLMANN, JAKOB BANDORF, NICKLAS VOLZ, ANDREAS FÖRNER, JOHANNES PRÖBSTLE, KERSTIN MULTERER, MATHIAS GÖKEN, MATTHIAS MARKL, STEFFEN NEUMEIER, and CAROLIN KÖRNER

Numerical methods can accelerate the design of alloys with improved material properties. One approach is the coupling of multi-criteria optimization with CALPHAD-based models of alloy properties. While this technique has already yielded promising new Nickel-base superalloys, the applicability to CoNi-base alloys has not yet been investigated. These alloys show promising properties for application as wrought high-temperature materials. We designed three CoNi-base superalloys, which were optimized for either high strength or high chemical homogeneity. The alloys were cast, and mechanical and thermophysical properties were characterized. The alloy optimized for strength showed creep performance inferior to a conventionally designed CoNi-alloy but had a much lower density. For developing highly homogeneous alloys, Scheil calculations were implemented in the optimization routine to quantify the severity of segregation. Non-equilibrium phases could be predicted successfully, resulting in a degree of homogeneity that rivaled that of a low-segregation ternary Co-base alloy. A comparison of elemental partitioning behavior and phase transition temperatures with CALPHAD calculations showed that trends are well represented for the most part. Finally, the applicability of the alloy design approach for Co-rich superalloys is evaluated, and possible applications for the optimized alloys are discussed.

https://doi.org/10.1007/s11661-022-06870-4

I. INTRODUCTION

SUPERALLOYS are the material of choice for applications in the hottest sections of aircraft engines and stationary gas turbines. This class of alloys exhibits excellent strength at high temperatures and strong resistance to creep deformation, as well as high oxidation and corrosion resistance. While Ni-base superalloys still dominate this field, especially as materials for turbine blades and disks in the first stages of a turbine, Co-base superalloys have attracted research interest in recent years. In both alloy systems, the ordered γ' phase ($L1_2$ structure) is crucial for the high-temperature strength. In Ni-base superalloys, this phase has the basic composition Ni_3Al, while Co-base superalloys form a γ' phase with a $Co_3(Al,W)$ composition. The γ' phase is coherently embedded in the disordered γ phase (fcc solid solution).

Research on Co-base superalloys has primarily been motivated by cobalt's ~ 40 K higher melting point compared to Ni, which can potentially increase the service temperature of thermal engines. However, the γ' solvus in Co-base superalloys may be up to 200 K lower than in Ni-base alloys, limiting the potential for usage above 1000 °C.[1] Furthermore, the two-phase γ/γ' region is quite narrow, which makes these alloys susceptible to forming detrimental intermetallic phases.[2,3] Solid solution strengthening elements tend to partition evenly between the γ and γ' phase or are, as in the case of W, even enriched in the γ' phase.[4] This is disadvantageous, if these alloys should be applied in the high temperature regime, where slowly diffusing elements in the γ matrix phase are necessary to reduce creep deformation. These issues can be alleviated by alloying with Ni, which widens the γ/γ' region, raises the

BENJAMIN WAHLMANN, MATTHIAS MARKL, CAROLIN KÖRNER are with the Department of Materials Science and Engineering, Institute II: Materials Science and Engineering for Metals (WTM), Friedrich-Alexander-Universität Erlangen-Nürnberg (FAU), Martensstr. 5, 91058 Erlangen, Germany. Contact e-mail: benjamin.wahlmann@fau.de. JAKOB BANDORF, NICKLAS VOLZ, ANDREAS FÖRNER, JOHANNES PRÖBSTLE, KERSTIN MULTERER, MATHIAS GÖKEN, STEFFEN NEUMEIER are with the Department of Materials Science and Engineering, Institute I: General Materials Properties, Friedrich-Alexander-Universität Erlangen-Nürnberg (FAU), Martensstr. 5, 91058 Erlangen, Germany.

Manuscript submitted August 5, 2022; accepted October 18, 2022.
Article published online November 16, 2022

γ' solvus temperature, and improves the partitioning behavior. Thus, many Co-base superalloys that are of scientific interest are, in fact, CoNi-base alloys.[5] However, with increasing Ni-content the beneficial, more homogeneous segregation on the dendritic scale of Co-base superalloys typically becomes less homogeneous.[6] This is unfavorable, since a low level of inhomogeneity is desirable to reduce the presence of casting defects and homogenization time of turbine blades or large forgings such as turbine disks.

Another drawback of the Co-base superalloys is their high W content. Advanced Co-base superalloys such as ERBOCo-1[5] or model alloys from the VF[7] and NC[1] series contain a significant amount of W between 4 and 10 at. pct to stabilize the γ' phase at elevated temperatures, though leading to a high density. This is unfavorable for applications as rotating parts such as turbine blades and disks.

Accordingly, we attempt to develop CoNi-base superalloys further in two directions by a computational alloy design approach. One aim is to develop alloys with improved creep strength, but reduced density. The second development strategy is to reduce the dendritic segregation while accepting a lower γ' solvus temperature.

Computational alloy design often employs machine learning methods[8–10] or CALPHAD (CALculation of PHase Diagrams) calculations to predict alloy properties.[11,12] Machine learning allows the prediction of phase stability or of phase transformation temperatures, density, and other properties of interest with high confidence, especially when combined with high-throughput experiments.[13,14] Such experiments are necessary to obtain the large amount of data necessary for reliable predictions. In contrast, CALPHAD databases are often readily available, covering a wide range of compositions, but the validity of predictions in certain composition ranges is not known a priori.

The predefined composition space is usually scanned systematically along a grid with regular spacing in the composition space, and relevant alloy properties are calculated. Finally, an alloy is selected by screening the calculated alloy properties for the composition which best fulfills the design requirements.[9,12,15] Alternatively, optimization algorithms may be used to evolve a population of compositions towards the desired properties.[16,17]

In this study, we employ the latter approach by coupling CALPHAD calculations to genetic multi-criteria optimization algorithms. We employ the numerical alloy design tool MultOpt + +[18–20] and its Python port PyMultOpt for the design process. In this framework, the alloy design task is defined as an optimization problem consisting of optimization goals that should be minimized or maximized and constraints that may not be violated. Such goals and constraints could be minimizing the alloy's density or setting a minimum value for its solidus temperature. Both programs employ genetic multi-criteria optimization algorithms to find a set of Pareto-optimal compositions that optimally satisfy the specified design goals. Each Pareto-optimal composition represents an optimal compromise solution to the alloy design problem in the sense that no criterion can be improved further without worsening another. Both tools have been applied in previous studies to design the lightweight, creep-resistant Ni-base superalloy ERBO/15[21] and to study the viability of solidification cracking criteria for the design of crack-resistant alloys for additive manufacturing.[22]

Here, we intend to explore the applicability of different computational design approaches to CoNi-base superalloys. The previously employed strategy for improving the creep resistance of Ni-base superalloys while minimizing their density relied on enhancing the partitioning of solid solution strengtheners to the γ matrix phase.[17,20] Since this strategy was highly successful, we investigate in the present study if this is also a viable strategy for designing CoNi-base superalloys that could be used at elevated temperatures. The resulting alloy is named ERBOCo-5.

Although CALPHAD allows only calculation of the thermodynamic equilibrium state, non-equilibrium solidification can be modeled by the Scheil–Gulliver model. Here, a local thermodynamic equilibrium is assumed at the solid–liquid boundary. This model provides an estimation of the degree of segregation and allows for predicting non-equilibrium phases. We apply Scheil-Gulliver solidification simulation in the optimization procedure to minimize the dendritic segregation to design CoNi-base superalloys that could be used as wrought alloys at medium temperatures, which requires also a wide temperature interval between γ' solvus and solidus temperature (processing window) to facilitate processing by forging,[23] while maintaining a suitable γ' fraction. Two alloys, ERBOCo-6 and -7, are designed.

The thermophysical and mechanical properties of the three optimized alloys are investigated in detail and compared to the conventionally developed Co-base alloy ERBOCo-1 to assess the viability of the numerical approach for the design of high-performance alloys.

The entire computational alloy design method rests upon the accuracy of the CALPHAD calculation predictions. Therefore, we compare our CALPHAD predictions to experimental measurements of the properties of the three CoNi-base superalloys that were selected based on our calculations to evaluate their reliability in the context of Co-rich alloy systems.

II. EXPERIMENTAL AND COMPUTATIONAL METHODS

A. *Property Models*

At the core of the numerical alloy design approach are property models, of which most rely on CALPHAD calculations to describe an alloy's mechanical and thermophysical properties. These calculations were carried out with the Thermo-Calc software versions 2017b/2020b using the databases TTNI8 (ThermoTech Ltd., Surrey, UK) and TCNI9 (Thermo-Calc, Solna,

Sweden). The alloy properties serve either as optimization goals or as constraints. In the following, we briefly describe the most important models.

1. *Density*

For the description of the density ρ in kg/m^3, a regression function developed by Caron[24] was used, taking into account the overall alloy composition:

$$\rho = 8296.04 - 65.95w_{Al} - 23.6w_{Ti} - 16.4w_{Cr} - 4.35w_{Co} + 12.95w_{Mo} + 54.41w_{Ta} + 62.47w_{W}, \quad [1]$$

with w_i indicating the weight percentage of an element.

2. *Solid solution strengthening index*

The solid solution strengthening index (I_{sss}) is an indicator of the creep resistance of an alloy at high temperature and low stress. It is derived from a study by Fleischmann *et al.*[25] on the solid solution hardening potential of Re, W, and Mo. It is defined as the weighted sum of the concentrations of Re, W, and Mo in the γ phase:

$$I_{sss} = 2.44x^{\gamma}_{Re} + 1.22x^{\gamma}_{W} + x^{\gamma}_{Mo} \quad [2]$$

where x denotes the proportion of an element in at. pct. These elements are differently effective in hindering dislocation movements, as indicated by their respective weighting factors. Despite its simplicity, this model has proved an adequate descriptor of high-temperature creep performance.[26]

3. *Misfit*

The misfit δ between the γ and γ' phase is defined as

$$\delta = \frac{a_{\gamma'} - a_{\gamma}}{\frac{1}{2}(a_{\gamma'} + a_{\gamma})} \quad [3]$$

with a_{γ} and $a_{\gamma'}$ as the lattice parameters of γ and γ' phase, respectively. Since molar volume is either not described at all (TTNI8) or not adequately (TCNI9) in the thermodynamic databases, regression functions by Caron[24] are used to calculate the lattice parameters in dependence on the phase compositions. Additionally, the different thermal expansion of the two phases is accounted for by considering the coefficients of thermal expansion of pure Ni and Ni_3Al.[27] This model was initially developed for Ni-base superalloys. No adaptation for Co-rich superalloys has been published. However, since the thermal expansion coefficients of α-Co[28] and Ni[29] as well as of Co-[30] and Ni-rich[31] $L1_2$ phases are of similar magnitude, we assume that this model is still generally applicable to CoNi-base superalloys.

Other properties employed in the optimization were calculated directly as thermodynamic properties of the respective systems, *e.g.,* phase fractions or phase transition temperatures.

B. *Numerical Alloy Design Procedure*

1. *Alloy design toolkit*

When designing an alloy, no single composition can typically satisfy all requirements optimally. It is more likely that some compositions fulfill only a part of the requirements well. In that case, a set of compositions exists among which no single property can be improved without worsening another. This set is the so-called Pareto front. The goal of our alloy design procedure is to find this composition set. Each member of the Pareto front represents an optimal compromise solution to the alloy design problem. Such Pareto fronts are usually constructed iteratively by evolutionary optimization algorithms. Since often multiple goals must be optimized at once, a multi-objective optimization algorithm is required.

Genetic optimization algorithms begin from a set of start points, which should be widely distributed over the entire composition search space. Goals and constraints are computed for each point, also called individual, and the best individuals are kept to create a new generation of test compositions to be evaluated. Thus, the computed Pareto front approaches the true Pareto front of the respective optimization problem with each iteration.

Computational alloy design was carried out by two implementations of our in-house developed optimization tool. The C++-based program MultOpt++[20] uses algorithms provided by the open source optimization library Geneva "Ivrea–Via Arduino" 1.6.1 by Gemfony Scientific. Specifically, a genetic optimization algorithm that was modified to employ a crowding distance sorting scheme for the selection of surviving individuals in each generation was employed. This scheme allows a uniform sampling of the Pareto front. Coupling to Thermo-Calc for calculating the goal and constraint functions is achieved via the TC-API.

The Python port of MultOpt++, PyMultOpt, uses the more recent TC-Python API to perform Thermo-Calc calculations. The algorithm NSGA-II[32] from the open source library pymoo[33] for multi-objective optimization is used for optimization. Start points were generated by Latin hypercube sampling. New candidate compositions were generated in each generation according to the simulated binary crossover scheme. It was verified that both tools yield the same result for a given optimization problem.

2. *Optimization of creep strength and density*

Co-base superalloys require a certain amount of γ' phase stabilizing elements. However, a high W content leads to a higher density than Ni-base superalloys. For usage as blades or disks in turbines, it is desirable to reduce the density by adjusting the W content to the minimum amount necessary to achieve an adequate γ' fraction and by employing other lighter γ'-stabilizing elements such as Al, Ti, and Ta. The primary optimization goal is therefore minimizing the density of the alloy. The density is constrained below 9000 kg/m^3 since any values above are undesirable.

We assume a target service temperature of 1100 °C for this alloy, ERBOCo-5. All temperature-dependent properties are assessed at this temperature. Since W and Mo are effective solid solution strengtheners, their partitioning to the γ phase should be maximal to ensure good creep resistance at the lowest possible density by maximizing the I_{sss}. However, this creep resistance indicator incorporates neither the effect of the γ' phase fraction nor that of the misfit. As the γ' fraction of the Ni-base superalloy CMSX-4 is widely considered nearly optimal, an additional constraint is introduced to keep the γ' fraction close to this value (about 45 mol pct). Nathal found an optimal creep resistance for γ' precipitates with a size of roughly 500 nm for a misfit between − 0.5 and − 0.1 pct for Ni-base superalloys.[34] In CoNi-base superalloys, the misfit transitions from positive to negative values with increasing Ni content.[1] Since the upper possible misfit value for this optimization problem was unknown, the misfit was restricted to a minimum of − 0.5 pct. Finally, introducing other γ' stabilizers, especially Ti, may reduce the solidus temperature below acceptable levels. We maximize the solidus temperature to counter this effect as a third optimization goal.

The full definition of the optimization task, including the composition range and further constraints to the density and the Co/Ni ratio, is summarized in Table I. The sum of γ and γ' phase fractions at 1100 °C is required to be greater than 99 mol pct to prohibit significant fractions of detrimental tertiary phases. Except for Co, the composition limits are adapted from the optimization of the Ni-base superalloy ERBO/15.[21] A minimum Cr content of 7.6 at. pct is enforced to ensure adequate corrosion resistance.

3. *Optimization of homogeneity and strength*

Elements that stabilize the γ' phase, such as Al and Ti, tend to partition to the liquid during solidification. If their concentration in the melt is too high, intermetallic phases may form that are difficult to dissolve by heat treatment. CoNi-base superalloys with a high Al content are especially prone to the formation of β-(Co,Ni)Al phase,[35] around which cracks form under load,[36] which ultimately decreases the stress-rupture lifetime.[37] Due to its brittleness, this phase is also expected to be detrimental to ductility and fatigue. The β phase is usually not revealed by CALPHAD calculations in thermodynamic equilibrium. However, it can be modeled well by Scheil calculations, where it occurs as a γ/β eutectic in the late stages of solidification. Forged superalloy parts such as turbine disks require high resistance against fatigue and a high degree of chemical homogeneity to ensure their structural integrity under complex loading conditions. Both these requirements can be optimized by minimizing the fraction of eutectic. Since a certain degree of segregation is necessary for eutectic to form, minimizing the eutectic fraction must also lead to chemically homogeneous alloys. Further, the fraction of eutectic was restricted to a maximum of 10 pct to drive the optimization towards technologically relevant compositions, as otherwise, the full range up to 100 pct eutectic would be explored.

Table I. Description of the Optimization Problem for ERBOCo-5. ρ, I_{sss}, T_{sol}, f_γ, $f_{\gamma'}$, and δ are the Density, Solid Solution Strengthening Index, Solidus Temperature, γ' Phase Fraction and Lattice Misfit Between γ and γ' Phase

Minimize	ρ
Maximize	I_{sss} (1100 °C)
Maximize	T_{sol}
	$\rho < 9000$ kg/m^3
	$T_{sol} > 1280$ °C
	43 mol pct $< f_{\gamma'}$ (1100 C) $<$ 47 mol pct
	f_γ (1100 °C) + $f_{\gamma'}$ (1100 C) > = 99 mol pct
	$\delta_{1100\ °C} > -0.5$ pct
Subject To	5 at. pct $< x_{Al} <$ 15 at. pct
	$x_{Ti} <$ 4 at. pct
	7.6 at. pct $< x_{Cr} <$ 12 at. pct
	35 at. pct $< x_{Co} <$ 60 at. pct
	$x_{Mo} <$ 6.5 at. pct
	$x_{Ta} <$ 3.5 at. pct
	$x_W <$ 3.5 at. pct
	$x_{Co} > x_{Ni}$

The eutectic fraction is calculated by the Scheil solidification model, where it is identified as the solid fraction interval in which two or more phases solidify simultaneously. Multicomponent Scheil simulations require a stepwise reduction of the temperature, at which equilibria are calculated, making them computationally intensive. The calculation procedure was therefore modified by increasing the temperature step adaptively to increase the computation speed.

As previously, the I_{sss} was maximized. Here, the I_{sss} was calculated at 900 °C since the service temperature of turbine disks is lower than that of blades. The γ' solvus temperature was maximized as a third design criterion to ensure an adequate amount of γ' precipitate phase, while keeping a processing window, i.e. the temperature difference between solidus and γ' solvus, larger than 75 °C. Al stabilizes both the γ' and the β phase. Therefore, a compromise must be found between a high γ' solvus temperature and a low/no β content.

Similar constraints as previously are applied to ensure that the Pareto-optimal compositions cover only the property ranges that are of interest for the application as a forged alloy. Additionally, the fraction of TCP phases (σ, μ, R, and P phase) at 900 °C was constrained below 1 mol pct. Co, Mo, Ta, and W concentration ranges were relaxed to avoid artificially limiting the maximum achievable I_{sss}. The full definition of the optimization problem is stated in Table II.

C. *Experimental Methods*

Single-crystalline rods with the respective alloy composition from Table III were produced using the Bridgman process at 3 mm/min withdrawal rate. The misorientation of the cast rods was determined by

Table II. Description of the Optimization Problem for ERBOCo-6 and -7. ρ, f_{eut}, I_{sss}, $T_{\gamma'}$, T_{sol}, and f_{TCP} are the Density, Fraction of Eutectic, Solid Solution Strengthening Index, γ' Solvus Temperature, Solidus Temperature, and the Fraction of TCP Phases

Minimize	f_{eut}
Maximize	I_{sss} (900 °C)
Maximize	$T_{\gamma'}$
	$f_{eut} < 10$ pct
	$\rho < 9000$ kg/m^3
	T_{sol}—$T_{\gamma'} > 75$ °C
	f_{TCP} (900 °C) < 1 mol pct
Subject To	5 at. pct < x_{Al} < 15 at. pct
	$x_{Ti} < 4$ at. pct
	7.6 at. pct < x_{Cr} < 12 at. pct
	10 at. pct < x_{Co} < 90 at. pct
	$x_{Mo} < 10$ at. pct
	$x_{Ta} < 10$ at. pct
	$x_W < 10$ at. pct
	$x_{Co} > x_{Ni}$

Table III. Nominal Compositions of ERBOCo-5, -6 and -7 in At. Pct

Alloy	Co	Ni	Al	W	Cr	Ti	Mo
ERBOCo-5	36.2	36.1	13.1	3.0	7.6	3.9	0.1
ERBOCo-6	37.3	36.7	9.6	2.1	7.6	0.8	5.9
ERBOCo-7	38.3	36.5	8.1	2.6	7.6	—	6.9

EBSD measurements. Using these measurements, ⟨001-oriented segments were extracted from the rods with a deviation within 5°. Samples for microstructure analysis and specimens for mechanical testing were prepared from these segments after solution annealing heat treatment at 1280 °C for 8 h and subsequent two-step aging heat treatment at 1050 °C for 5 h (ERBOCo-5 & -7) or 3 h (ERBOCo-6) and finally at 900 °C for 16 h in vacuum. The cooling rate between the three heat treatment temperatures and from the last aging to room temperature was approximately 300 °C/h. Additional heat treatments at temperatures from 750 °C up to 1163 °C (steps of 50 °C) were performed for 24 h in air, followed by water quenching in each case to determine the γ' volume fraction as a function of the temperature. After standard metallographic sample preparation with a final chemical mechanical polishing (additional electrolytic polishing of ERBOCo-5 samples), the microstructure was characterized using backscattered electron (BSE) imaging using *Zeiss Cross Beam 1540 EsB, Zeiss Cross Beam 540, and Helios NanoLab 600i* (*Thermo Fisher Scientific*) scanning electron microscopes (SEM). The area fraction of the B2 phase (only in ERBOCo-5) and the γ' phase, as well as the shape factor of the γ' precipitates, were determined from binarized images using *ImageJ* software. The γ' volume fractions were calculated from the measured area fractions according to the approach developed by Giese.[38]

EPMA measurements were performed using a *Jeol JXA 8100* to characterize the elemental distribution in the as-cast state of all three alloys. The mappings were acquired over an area of 0.5 × 0.5 mm (ERBOCo-5) and 1 × 1 mm (ERBOCo-6/-7) with a step size of 2.5 μm and 5 μm. From that, segregation profiles were determined by sorting the compositions according to the rank-sort method of Ganesan *et al.*[39] The Scheil-Gulliver equation (Eq. [4]) was then fitted to these profiles,[40] from which the segregation coefficient k for each alloying element can be derived as

$$c_S = kc_0(1 - f_s)^{k-1}, \quad [4]$$

where c_s denotes the elemental concentration in the solid, c_0 the nominal composition, and f_s the corresponding solid fraction. For ERBOCo-5, the concentration profiles were only evaluated up to a solid fraction f_s of 90 pct, since the precipitation of the B2 phase caused a kink in the curves that would distort the fit.

The γ' solvus temperature and the solidus and liquidus temperatures of the three alloys were determined by differential scanning calorimetry (DSC) using samples with a diameter of about 4 mm and a thickness of about 1 mm in a *Netzsch 404 F1 Pegasus* (ERBOCo-5) and a *Netzsch STA409* (ERBOCo-6/-7). Measurements were performed up to 1500 °C with heating and cooling rates of 5 °C/minute between 800 °C and 1500 °C.

Atom Probe Tomography (APT) was performed to determine the concentrations of the individual elements in the γ matrix and the γ' precipitates. APT specimens were prepared by in-situ lift-out using a *Zeiss Crossbeam 540 FIB/SEM* as described in References 41 and 42. The APT experiments were carried out in a CAMECA LEAP 4000X HR (CAMECA Inc.) using pulsed laser mode to trigger field evaporation. A UV laser with 355 nm wavelength at a pulse energy of 50 pJ was used. The temperature was set to 49 K, and a pulse repetition rate of 125 kHz was applied. Data processing was done using the commercial software IVAS 3.6.8 from CAMECA Inc. From the quantified elemental compositions in the γ (c_γ) and γ' ($c_{\gamma'}$), the partitioning coefficients $k_i^{\gamma'/\gamma}$ of the elements were calculated according to (Eq. [5]). The concentration of the γ' phase was taken only from the primary γ' precipitates.

$$k_i^{\gamma'/\gamma} = \frac{c_{i,\gamma'}}{c_{i,\gamma}} \quad [5]$$

Compression tests were performed up to a temperature of 1000 °C at a constant strain rate of 1.0×10^{-4} s^{-1} using cylindrical samples with a diameter of about 3 mm and a height of about 4.5 mm to determine the temperature-dependent compression flow stress of the alloys. Compression creep tests were performed at 900 °C and 250 MPa using cylindrical samples with a diameter of about 4.5 mm and a height of about 7 mm.

The conventionally developed CoNi-base superalloy ERBOCo-1, which has been well investigated in numerous studies,[5,43,44] was taken as a reference alloy to evaluate the experimental results of the numerically designed alloys ERBOCo-5, -6 and -7.

III. RESULTS

A. *Alloy Selection*

The Pareto fronts that resulted from the optimization of alloy properties are presented in Figures 1 and 2.

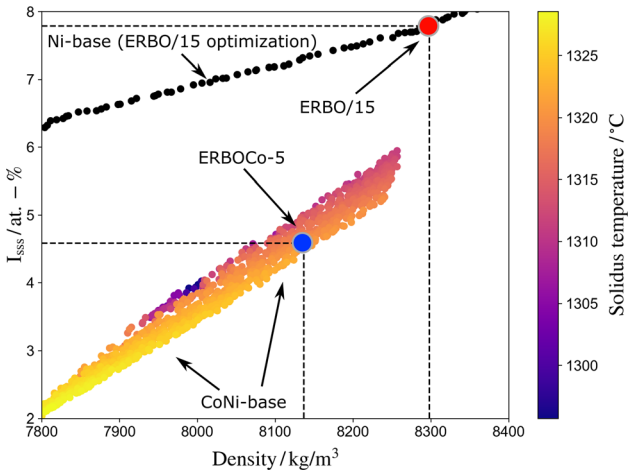

Fig. 1—Pareto front representing the maximum possible solidus temperature and solid solution strengthening index I_{sss} while minimizing the density. For comparison, the maximum attainable I_{sss} for Ni-base alloys and the location of ERBO/15 are also depicted.

Each Pareto front comprises about 1000 individual compositions. Among these compositions, only a few are selected for further experimental investigation. In principle, all compositions on the Pareto front are optimal. One must apply a suitable selection method to choose one or more compositions for the desired application. The compositions and selected calculated properties of the three chosen alloys are given in Table III.

The alloy ERBOCo-5 was selected from the Pareto front resulting from the optimization of creep strength (i.e. the I_{sss}) and density (Figure 1). Only solutions with a density greater than 7800 kg m^{-3} are shown here, since alloys below this threshold possess I_{sss} values too low to be of interest for experimental investigation. A higher I_{sss} can be achieved by accepting a higher density. The solidus temperature decreases with both increasing I_{sss} and density. As the definition of the optimization problem was inspired by the previous development of the Ni-base superalloy ERBO/15, the selection criteria were chosen similarly. For comparison, the maximum attainable I_{sss} dependent on the density for the optimization leading to ERBO/15 is also presented. The candidate compositions were first reduced by excluding all compositions with a solidus temperature below 1320 °C, which was the minimum permissible solidus temperature for ERBO/15. Among the remaining candidates, the composition with the highest I_{sss} was selected.

We selected two alloys from the optimization of homogeneity and strength to investigate the influence of the choice of the eutectic fraction on the alloys' homogeneity. The associated Pareto front (Figure 2) features two regions that can be distinguished visually. One comprises low to medium solid solution

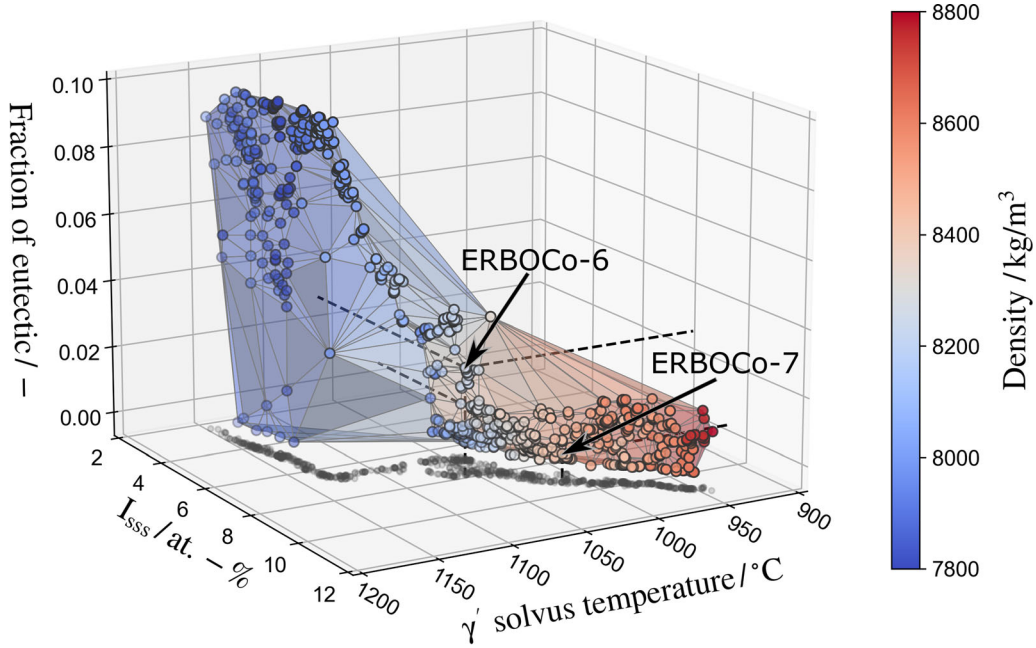

Fig. 2—Pareto front for minimization of eutectic fraction and maximization of solid solution strengthening index I_{sss} and γ' solvus temperature. The projection of the Pareto front onto the bottom plane highlights its structure. The color indicates the density. Dashed lines mark the locations of the selected alloys (Color figure online).

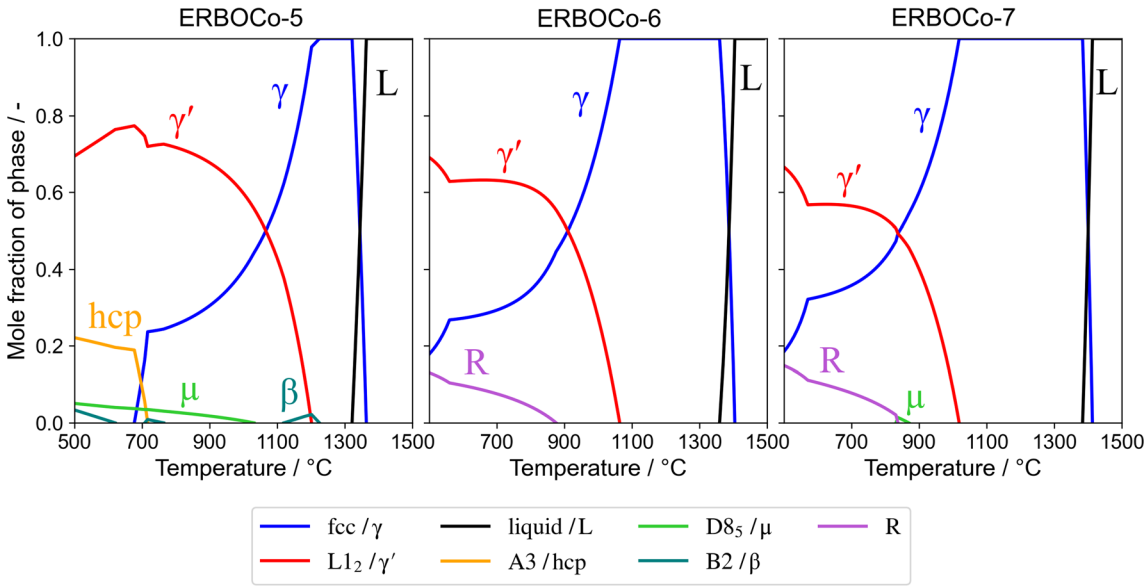

Fig. 3—Calculated phase diagrams of the experimental alloys using the databases TTNI8 (ERBOCo-5) and TCNI9 (ERBOCo-6/-7).

strengthening, high γ' solvus temperature, and a comparatively high eutectic fraction. In the second region, where the I_{sss} is comparatively high, the γ' solvus temperature is low, and the fraction of eutectic is mainly below 2 pct. Since there is no empirical data as to which values of eutectic fraction are appropriate for sufficient homogeneity, which was the principal goal of the optimization, we turned to the trade-off metric proposed by Rachmawati to select alloys for experimental analysis.[45] For a pair of points X_i and X_j, the trade-off T is defined as the ratio between aggregated improvement and aggregated deterioration:

$$T = \frac{\sum_{m=1}^{M} max\left(0, f_m(X_j) - f_m(X_i)\right)}{\sum_{m=1}^{M} max\left(0, f_m(X_i) - f_m(X_j)\right)} \quad [6]$$

with the number of optimization goals M and the goal function values f. The trade-off is calculated for each pair of Pareto-optimal points and for each point, the minimum of all respective trade-off values is chosen. This metric identifies convex bulges on the Pareto front. These solutions are interesting choices among the Pareto-optimal points since they yield the greatest improvement per unit degradation. Solutions with a high value of the trade-off metric offer a balanced compromise between the optimization goals.

From each of the two regions of the Pareto front, the alloy with the highest trade-off metric was selected: ERBOCo-6 from the high-eutectic region, ERBOCo-7 from the low-eutectic region.

The phase fractions in dependence on temperature and the Scheil solidification curves of the selected alloys are presented in Figures 3 and 4, respectively. The calculations were carried out with the respective thermodynamic databases employed for the optimization. Calculated fundamental properties that served as goals and constraints in the optimizations are summarized in Table IV.

The predicted γ' solvus temperature of ERBOCo-5 (1202 °C) is the highest of all developed alloys. Thus, it is also higher compared to that of other experimental Co and CoNi-base superalloys such as VF100 (1121 °C),[7] ERBOCo-1 (1174 °C),[5] ,or the alloys L12-L19 developed by Lass *et al.* (up to 1167 °C).[46] The calculated γ' solvus temperatures of ERBOCo-6 and -7 are considerably lower (1064/1019 °C), which puts them into the neighborhood of conventional forged Ni-base superalloys such as Waspaloy (~ 1050 °C)[47] or René 41 (~ 1070 °C)[48] or other experimental polycrystalline CoNi-base superalloys such as CoWAlloy1 and CoWAlloy2.[23]

The densities of all alloys are below 8450 kg/m^3 and thus notably lower than that of other CoNi-base superalloys, such as ERBOCo-1 (~ 9200 kg/m^3) and the CoWAlloys (~ 8800 kg/m^3), or the Ni-base superalloy CMSX-4 (~ 8700 kg/m^3) and comparable to forged Ni-base alloys (~ 8200 kg/m^3). This is mainly due to the relatively high Al content and the low fraction of W. In ERBOCo-6 and -7, Mo is the primary solid solution strengthening element. A high I_{sss} can be achieved through the high Mo content, as W is only 22 pct more efficient in strengthening according to the I_{sss} definition, while its density is nearly twice as high. However, the advantage of Mo's low density is partially offset by the lower Al content in ERBOCo-6 and -7, which is required to avoid the formation of the B2 phase in a eutectic reaction. Therefore, the overall density of these alloys is higher than that of ERBOCo-5.

The two Mo-rich alloys also exhibit a high fraction of R phase below ~ 850 °C. This is a consequence of the high Mo content stabilizing the R phase.[49] Since precipitation of TCP phases is usually sluggish, and the diffusion rate is low at temperatures where significant fractions of R phase occur, no significant fractions of R phase are expected in practice. However, it is unclear how accurate the description of TCP phases in

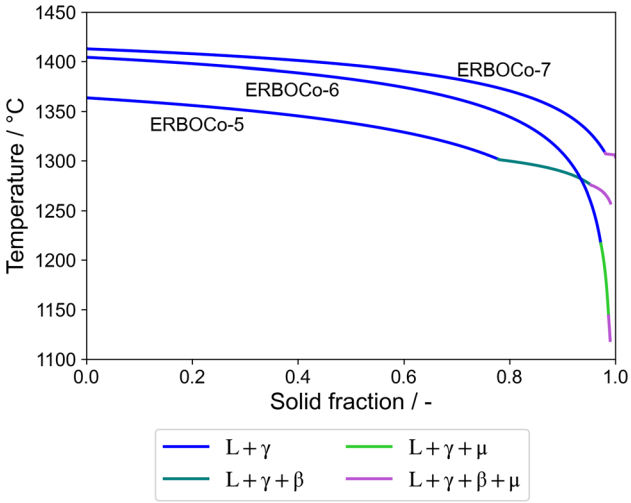

Fig. 4—Calculated Scheil solidification curves of the experimental alloys using the databases TTNI8 (ERBOCo-5) and TCNI9 (ERBOCo-6/-7).

Table IV. Calculated Fundamental Properties of ERBOCo-5, -6, and -7: Density ρ, Solid Solution Strengthening Index I_{sss}, γ' Solvus Temperature $T_{\gamma'}$, Solidus Temperature T_{sol}, and the Fraction of Eutectic f_{eut}

Alloy	ρ in kg/m^3	I_{sss}	$T_{\gamma'}$ in °C	T_{sol} in °C	f_{eut} in Pct
ERBOCo-5	8137	4.58 (1100 °C)	1202	1321	22.1
ERBOCo-6	8253	8.26 (900 °C)	1064	1359	2.7
ERBOCo-7	8421	9.63 (900 °C)	1019	1384	0.3

the employed databases is due to the difficulty of obtaining reliable thermodynamic data for these slowly precipitating phases.

The solidification sequences of all alloys begin with the formation of the γ phase from the melt (Figure 4). In ERBOCo-5, the formation of β-(Co,Ni)Al in parallel with the γ phase is predicted, starting from a solid fraction of 78 pct. Finally, also μ phase forms. For ERBOCo-6 and -7, single-phase solidification is predicted up to 97 and 98 pct, respectively, corresponding to 3 and 2 pct of eutectic. The single-phase solidification is followed by the formation of small amounts of β or μ phase. It should be noted that the eutectic fractions directly calculated with Thermo-Calc, especially of ERBOCo-7, deviate slightly from the ones calculated during the optimization due to the modification of the Scheil solidification model. Nevertheless, the order of eutectic fractions is not changed.

B. *Microstructure*

The microstructures of the three investigated alloys ERBOCo-5, -6 and -7 in the as-cast state and after solution and aging treatment are shown in Figure 5. All alloys exhibit a typical dendritic microstructure in the as-cast state. Intermetallic precipitates are present within the as-cast microstructure. However, there are significant differences between ERBOCo-5 on the one side and ERBOCo-6 and ERBOCo-7 on the other. ERBOCo-5 shows a strongly pronounced dendritic microstructure and a high amount of eutectic intermetallic precipitates in the interdendritic regions (Figure 5(a)). The intermetallic phase was identified as B2-phase by electron backscatter diffraction (EBSD) and energy dispersive X-ray spectroscopy (EDX). Its area fraction was measured at 8.6 ± 0.6 pct. In contrast, ERBOCo-6 and -7 show a relatively homogenous as-cast microstructure with a much less pronounced dendritic structure, where single dendrites can hardly be distinguished (Figure 5(b) and (c)). Moreover, only minimal and negligible fractions of eutectic intermetallic phases are present in the as-cast state with such small amounts that it was impossible to determine an area fraction of these phases. Despite the high predicted equilibrium fraction of R phase in ERBOCo-6 and -7 at a lower temperature, no R phase was found.

After solution and aging heat treatment, a two-phase γ/γ' microstructure without additional intermetallic phases has formed in ERBOCo-6 and -7 (Figures 5(e) and (f)). The γ' volume fraction is 49 ± 5 pct in ERBOCo-6 and 36 ± 4 pct in ERBOCo-7, respectively. Furthermore, γ' precipitates are homogeneously distributed within the γ matrix phase, exhibit a rather cubic shape, and a precipitate size of 132 ± 55 nm in ERBOCo-6 and 68 ± 19 nm in ERBOCo-7, respectively. In contrast, the B2 intermetallic phase has not vanished entirely after complete heat treatment in ERBOCo-5. It still occurs as blocky particles in the interdendritic areas, besides the γ/γ' microstructure (inset in Figure 5(d)). The γ' volume fraction with 80 ± 2 pct as well as the γ' particle size with 821 ± 242 nm are considerably greater in ERBOCo-5 than in ERBOCo-6/-7. The γ' precipitates seem to be irregularly aligned to each other and inhomogeneously distributed within the γ matrix. Some of the precipitates seem to be grown together with an irregular shape. The γ' particles are rather round compared to ERBOCo-6 and ERBOCo-7, indicating a lower lattice misfit at the second aging temperature of 900 °C.

C. *Segregation Behavior*

The solid composition as a function of the solid fraction for the three investigated alloys is shown in Figure 6. The Scheil Eq. [4] fits to the concentration curves are indicated by dashed lines. From these fits, microsegregation coefficients were derived (Figure 7). For ERBOCo-5, the profiles were only fitted up to a solid fraction of 90 pct where a kink appears. This kink is related to the formation of the Al-rich B2 phase and cannot be adequately described by the analytical Scheil equation, which requires the presence of a single solid phase. The location of the kink allows estimating the area fraction of B2 phase at about 10–12 pct. Furthermore, the segregation of Mo was not evaluated, as it was hardly measurable due to its low concentration.

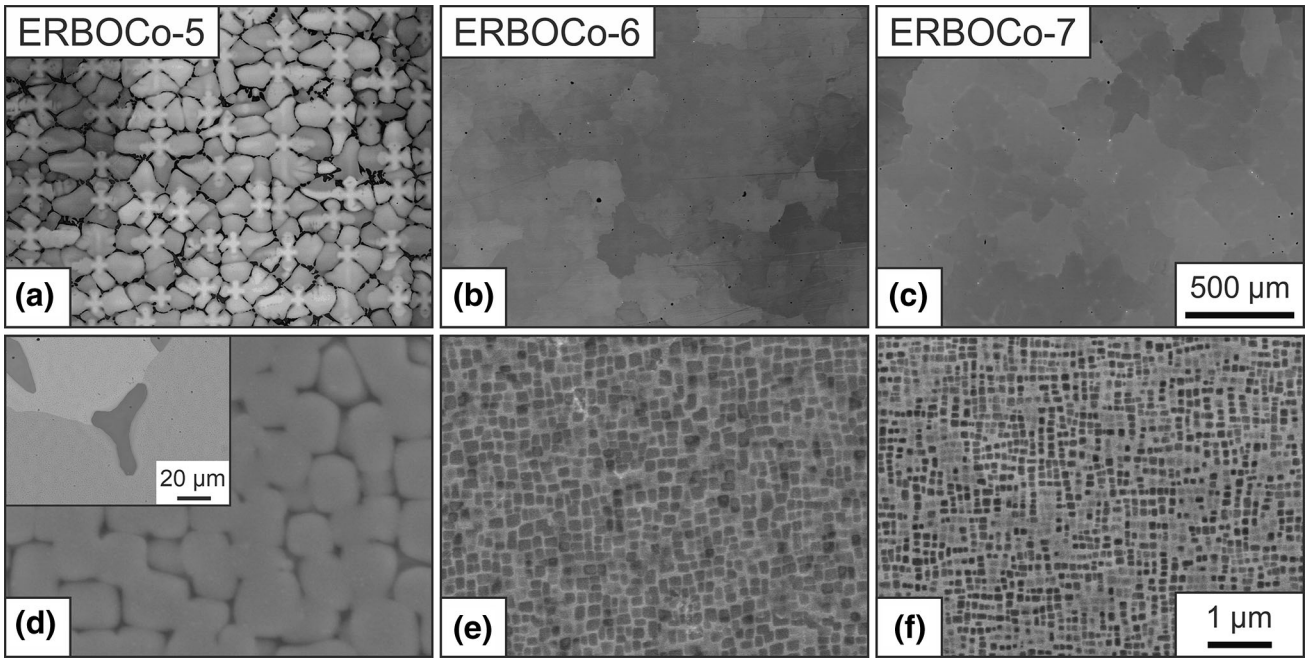

Fig. 5—SEM images from backscattered electron (BSE) mode of (*a*), (*d*) ERBOCo-5, (*b*), (*e*) ERBOCo-6 and (*c*), (*f*) ERBOCo-7 alloy in the (a) to (c) as-cast state and (d) to (f) after solution and aging heat treatment. The inset in (d) shows the microstructure of ERBOCo-5 in the fully heat-treated state at lower magnification with the apparent B2 phase.

While strong elemental partitioning occurs in ERBOCo-5 due to the precipitation of the intermetallic phase, the segregation profiles on ERBOCo-6 and -7 exhibit only a gentle slope. Slight partitioning, especially of Mo, is apparent. However, the overall degree of homogeneity is far greater than in ERBOCo-5. These findings confirm the SEM observations of both alloys' very homogeneous dendritic microstructure in the as-cast state (Section III–B).

In general, ERBOCo-5 exhibits a similar elemental segregation behavior as the conventionally developed ERBOCo-1 superalloy with Co and Cr being slightly, and W strongly enriched in the dendrite cores (DC). Ni and Al are slightly, and Ti is strongly enriched in the interdendritic regions. The segregation coefficients of Co and Ti are equal in both alloys. In contrast, the segregation coefficients of Ni, Al and Cr are slightly higher, and the segregation coefficient of W is considerably higher in ERBOCo-5 compared to ERBOCo-1. Microsegregation of the elements in ERBOCo-6 and ERBOCo-7 is significantly reduced compared to ERBOCo-5 and ERBOCo-1. The segregation coefficients of Co and Al are even closer to 1 than the ones in the ternary Co-9Al-9 W alloy that already has a very low degree of microsegregation, which was studied by Koßmann *et al.*[6] Segregation of elements in ERBOCo-6 is a little less pronounced than in ERBOCo-7, except for W. The segregation coefficient of Al is nearly unity and is thus not visible in Figure 7. The segregation behavior of Ni and Cr is reversed in both alloys, though with negligible deviation from unity. The segregation coefficient of Co is slightly, and the coefficient of W is strongly reduced compared to ERBOCo-5.

D. *Thermophysical Properties*

The density of the four alloys ERBOCo-1, -5, -6 and -7 is shown in Figure 8. The density of the conventionally developed ERBOCo-1 is the highest one amongst these alloys, exceeding 9000 kg/m^3. ERBOCo-5 has the lowest density with about 8300 kg/m^3, and ERBOCo-6 and -7 show a nearly equal density of about 8800 kg/m^3. The three alloys meet the respective constraints of a density lower than 8400 kg/m^3 for ERBOCo-5 and lower than 9000 kg/m^3 for ERBOCo-6 and -7 (see Section II–C). The regression model can reproduce the trends in density; however, the densities of the experimental alloys are consistently underestimated. The model's inaccuracy in this composition range is probably due to great compositional differences to the Ni-base alloys that were used to build the model.

Figure 9(a) shows the transformation temperatures obtained by DSC and thermodynamic calculations. The γ' solvus temperature of 1163 °C in ERBOCo-5 is the highest among the three numerically designed alloys and is close to the one of the conventionally developed ERBOCo-1 alloy. ERBOCo-6 and -7 exhibit a much lower γ' solvus temperature of 1040 °C and 986 °C, respectively. The difference in solvus temperatures can be attributed to the chemical composition of the alloys. The concentration of γ' forming elements such as Al, W, and Ti is significantly reduced in ERBOCo-6 and -7 compared to ERBOCo-5. In contrast, both the solidus temperatures of 1384 °C and 1401 °C and the liquidus temperatures of 1412 °C and 1426 °C are nearly equal in ERBOCo-6 and -7. They are higher than ERBOCo-5 with 1302 °C (solidus) and 1361 °C (liquidus). For ERBOCo-5, the optimization goal of a high solidus

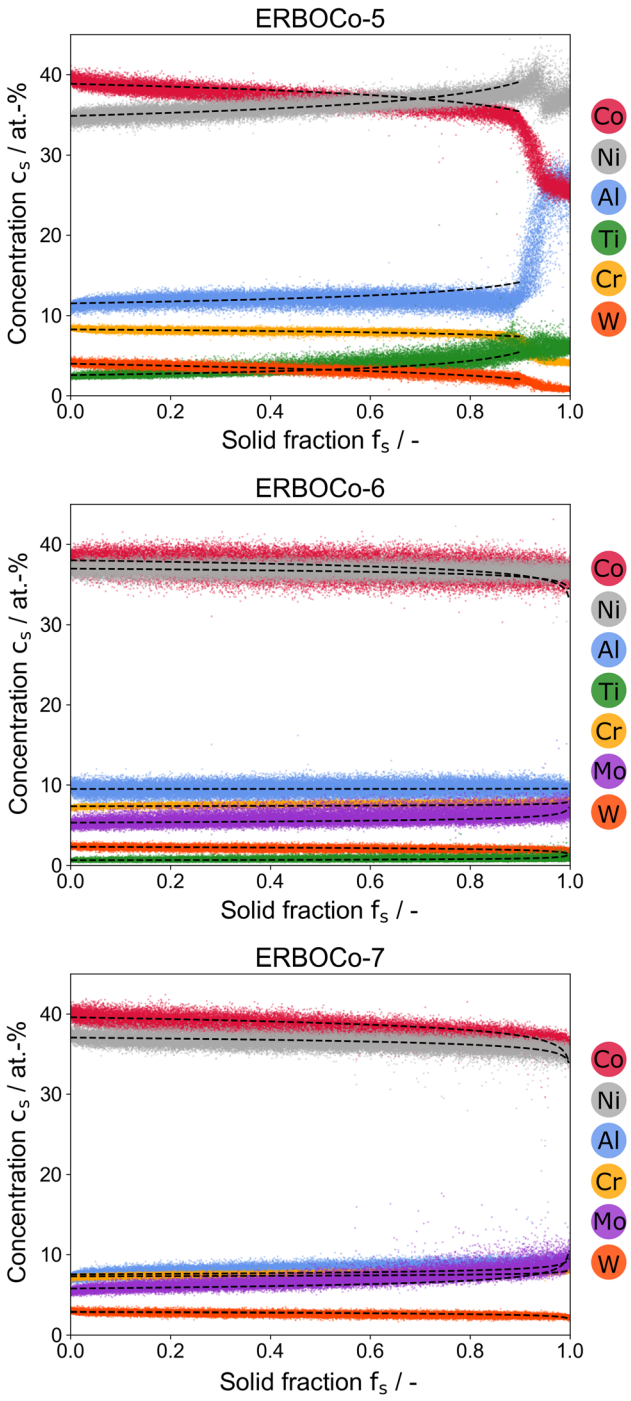

Fig. 6—Solid compositions of the investigated alloys ERBOCo-5, -6, -and -7 obtained by EPMA in dependence on the solid fraction. The fits of the Scheil equation to the curves are shown as dashed lines.

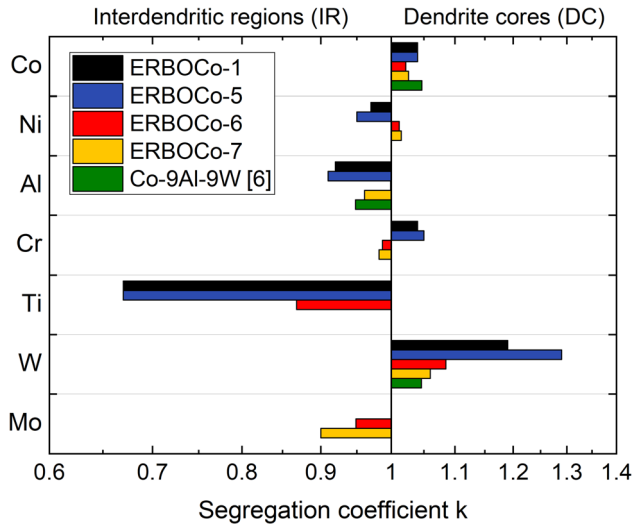

Fig. 7—Microsegregation coefficients for the investigated alloys ERBOCo-5, -6, -7 and the conventionally developed ERBOCo-1 CoNi-base superalloy. The segregation coefficients for the ternary Co-base superalloy Co-9Al-9 W (at. pct) taken from Koßmann *et al.*[6] are also shown for comparison.

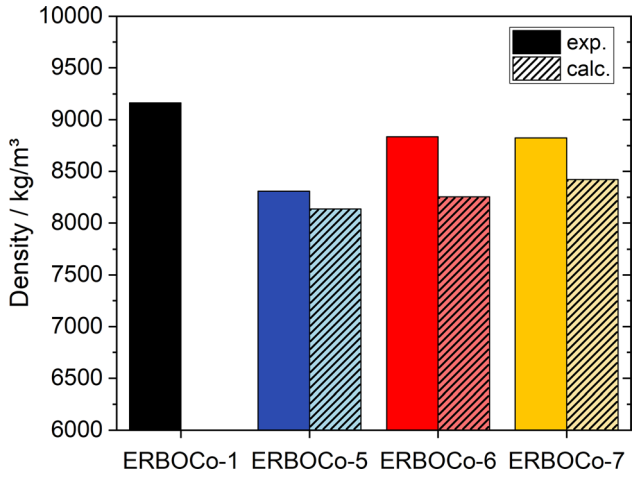

Fig. 8—Density of ERBOCo-5, -6 and -7 compared to the conventionally developed ERBOCo-1 CoNi-base superalloy and calculated values.

temperature ($T_{sol} > 1280$ °C) was achieved. For ERBOCo-6 and -7, the differences between γ' solvus temperature and solidus temperature of 344 °C and 420 °C, respectively, are high and therefore, the constraint of a sufficient heat treatment and processing window (T_{sol}—$T_{\gamma'} > 75$ °C) is fulfilled.

Thermodynamic calculations describe the trend of the transformation temperatures between the three alloys qualitatively well. The absolute values of the γ' solvus temperatures are slightly overestimated, whereas the solidus and liquidus temperatures are slightly underestimated for all three alloys regardless of the database used for the calculations (ERBOCo-5: TTNI8; ERBOCo-6/-7: TCNI9). However, deviations from the experimentally determined transformation temperatures are quite low and of similar magnitude for both databases. The difference between experimentally and thermodynamically calculated values is below 40 °C for the γ' solvus temperatures and even lower for the solidus and liquidus temperatures, with a maximum difference of 20 °C.

The γ' volume fraction as a function of the temperature is presented in Figure 9(b). No calculations for ERBOCo-1 are included, since our databases produced unreasonable results for this alloy. Starting from an

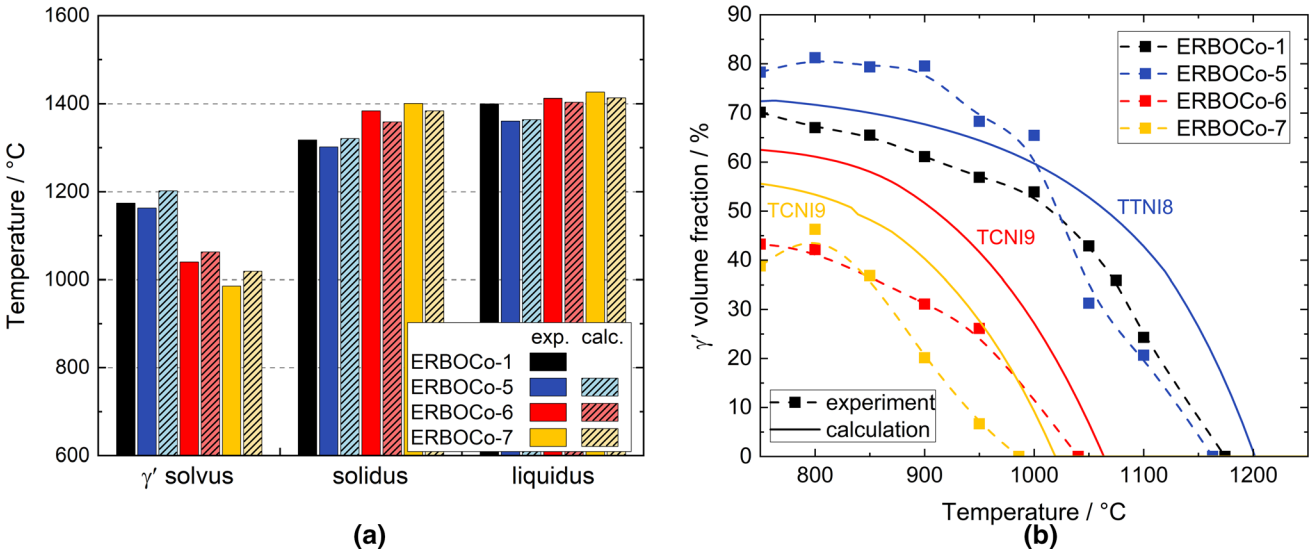

Fig. 9—(*a*) Transformation temperatures for the alloys ERBOCo-1, -5, -6 and -7 (solid: experimental data, hatched: calculated data) and (*b*) γ' volume fraction of ERBOCo-1, -5, -6, -7 as a function of temperature (dashed lines: experimental data, solid lines: calculated values).

initial volume fraction of 80 pct at room temperature (Section II–B) in ERBOCo-5, the volume fraction stays nearly constant at about 80 pct in the temperature range from 750 °C to 900 °C. With increasing temperature, the volume fraction slightly decreases to 65 pct at 1050 °C before it strongly decreases towards 0 pct at higher temperatures up to the γ' solvus temperature. The decrease in volume fraction at elevated temperatures is more pronounced than in EROBCo-1. With a volume fraction of only 21 pct at 1100 °C, the optimization constraint of 43 to 47 mol pct γ' at this temperature is not fulfilled. The thermodynamically calculated values (TTNI8 database) underestimate the volume fraction at temperatures below 1000 °C, whereas the volume fraction is considerably overestimated by up to 20 pct at temperatures above 1000 °C. Despite a difference in the γ' volume fraction of 13 pct at room temperature, ERBOCo-6 and -7 both exhibit a similar volume fraction of about 40 pct in the temperature range of 750 °C to 850 °C. The volume fraction is only about half of that of ERBOCo-5 due to the lower concentration of γ' forming elements like W, Al, and Ti. At higher temperatures, the volume fraction of ERBOCo-7 decreases stronger with increasing temperature compared to ERBOCo-6 due to its lower γ' solvus temperature. Although a different database was used for the calculations of these alloys (TCNI9), the volume fraction of ERBOCo-6 and -7 is strongly overestimated by the thermodynamic calculations in the considered temperature range. The deviation in γ' fraction up to 20 mol pct is similar to ERBOCo-5.

The partitioning of elements, especially solid solution strengtheners such as Mo and W, is crucial for efficiently using all alloying components. The partitioning coefficients between the γ and γ' phase were calculated from APT measurements and with CALPHAD at 800 °C (Figure 10). We assume that this temperature adequately represents the state in which the APT

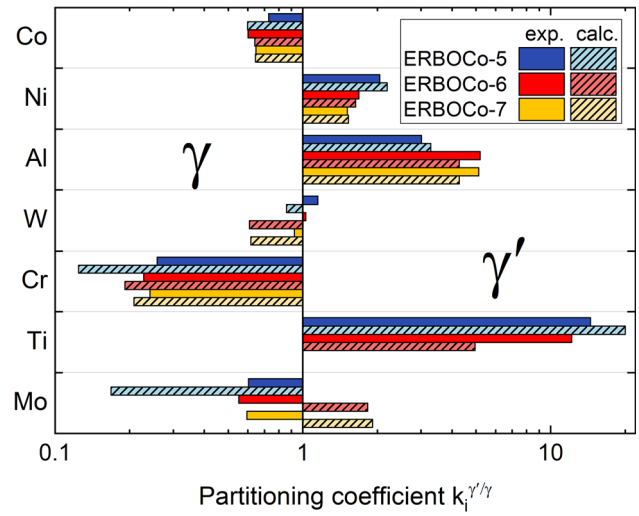

Fig. 10—Elemental partitioning between γ and γ' phase (solid: experimental data, hatched: calculated data). Calculations were carried out using the databases TTNI8 (ERBOCo-5) and TCNI9 (ERBOCo-6/-7).

measurements were carried out since changes in phase composition occur slowly below this temperature. Only γ and γ' phases were included in the calculations, as these are the only phases observed in the microstructure.

The calculated partitioning coefficients of Co, Ni, Al, Cr, and Ti in ERBOCo-5 match the measured values well. Cr shows a medium deviation. The TTNI8 database severely overestimates the enrichment of Mo in the matrix. However, due to the small fraction of Mo in the alloy (0.1 at. pct), there is some uncertainty regarding the accuracy of the measurement. For W, the prediction is even worse, as the calculated partitioning is the reverse of the measured one. W is nearly equally concentrated in both phases since it stabilizes the γ' phase.

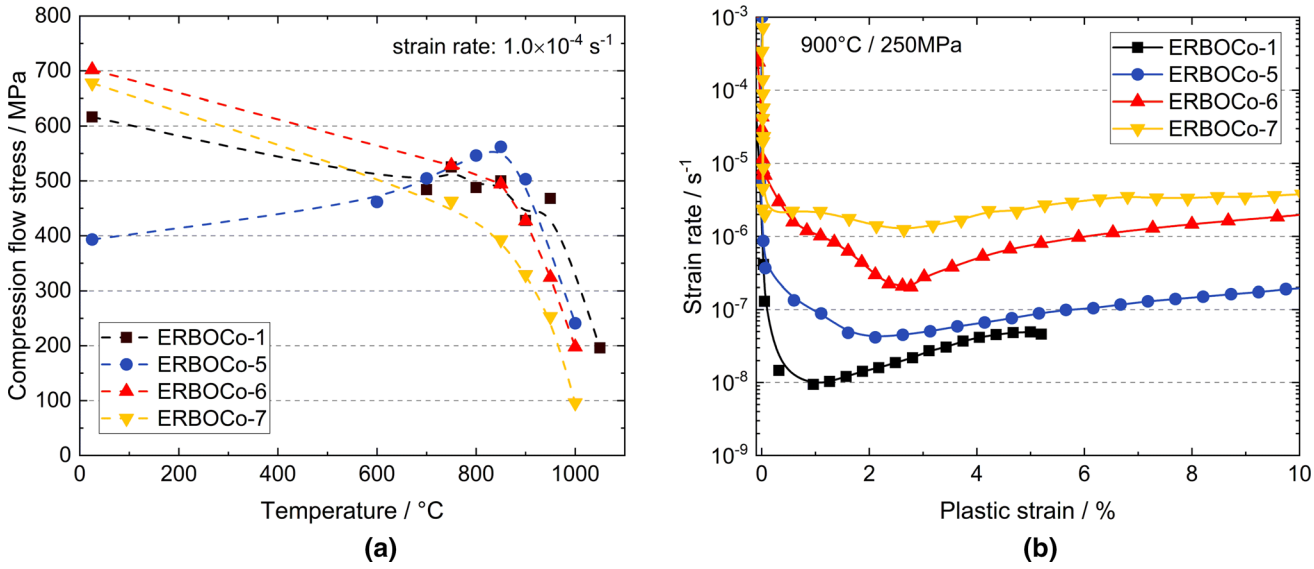

Fig. 11—(*a*) Compressive flow stress of ERBOCo-1, -5, -6 and -7 as a function of temperature (*b*) Creep curves of ERBOCo-1, -5, -6 and -7 at 900 °C and 250 MPa.

For ERBOCo-6 and -7, the predicted partitioning coefficients of Co, Ni, Al, and Cr also agree well with the measurements. According to the APT measurement, Ti partitions more strongly to the γ' phase than the calculation suggests. For the refractories Mo and W, the picture is again quite different. In the case of W, the calculations predict a far stronger partitioning than was measured. For ERBOCo-6, the partitioning behavior is reversed as for ERBOCo-5. This is also the case for Mo, where the APT measurements show partitioning to the γ matrix, while the TCNI9 database predicts partitioning to the γ' phase. This disagreement is quite surprising, given that maximization of the I_{sss} should optimize the partitioning of solid solution strengtheners towards the γ matrix.

The remaining elements are partitioned as expected between the phases. Al and Ti are γ' formers and are enriched in this phase. Enrichment of Cr and Co in the γ phase is often observed in Co-base superalloys,[50] as well as partitioning of Ni to the γ' precipitates.[51]

E. *Mechanical Properties*

The compressive flow stress of ERBOCo-1, -5, -6 and -7 as a function of temperature is shown in Figure 11a). At room temperature, ERBOCo-6 exhibits the highest compressive flow stress with about 700 MPa, which is slightly higher than the one of ERBOCo-7 and also higher than the flow stress of ERBOCo-1 reference alloy. The compressive flow stress in ERBOCo-5 with about 400 MPa is significantly lower than in ERBOCo-6 and -7. This difference can be attributed to the γ' particle size and the chemical composition. Despite a lower γ' volume fraction, the γ' particle size in ERBOCo-6 and -7 is very small compared to ERBOCo-5 and therefore, the strengthening contribution of the γ' phase is stronger. Additionally, the γ' precipitates are well aligned, have a regular shape, and are homogeneously distributed within the matrix phase. Moreover, despite a slightly lower W content, ERBOCo-6 and -7 contain more Mo than ERBOCo-5. As molybdenum is a highly effective solid solution strengthening element in superalloys and is enriched in the matrix (Figure 10), it impedes the deformation of the γ matrix phase. It hence leads to higher compressive flow stress. Furthermore, the exceptionally high γ' volume fraction of 80 pct and an irregularly shaped and aligned γ' phase could also cause the significantly lower compressive flow stress of ERBOCo-5 at room temperature.

With increasing temperature, the compressive flow stress of ERBOCo-6 and -7 steadily decreases, and no flow stress anomaly can be observed. The flow stress of ERBOCo-6 is higher than ERBOCo-7, most likely due to its higher γ' volume fraction. In contrast, ERBOCo-5 shows a pronounced flow stress anomaly. Its flow stress strongly increases with higher temperature and exceeds the values of ERBOCo-7 at 700 °C and ERBOCo-1 and -6 at 800 °C, respectively. It reaches a maximum value of about 550 MPa at 850 °C. The anomalous behavior of flow stress at high temperatures in γ'-strengthened superalloys is often attributed to the formation of Kear-Wilsdorf (KW)-locks in the $L1_2$-ordered γ' particles. Since ERBOCo-5 exhibits a high γ' volume fraction, a much higher number of KW-locks can likely form compared to the other two alloys in which no flow stress anomaly can be observed. Furthermore, the γ' particle size that strongly varies between the alloys may also influence the formation and effectiveness of strengthening by KW-locks. However, the specific deformation mechanisms of the alloys have not been studied in detail. At even higher temperatures, the flow stress of ERBOCo-5 sharply decreases and falls below that of ERBOCo-1. However, it is still higher than the flow stress of ERBOCo-6 and -7 at 1000 °C.

The compression creep curves of ERBOCo-1, -5, -6 and -7 at 900 °C and 250 MPa are presented in Figure 10(b). ERBOCo-7 shows the highest creep rates, i.e., the lowest creep strength, of all four alloys. The

creep rates of ERBOCo-6 are lower than in ERBOCo-7, which is also expected from the higher γ' volume fraction and compressive flow stress at 900 °C. The creep rates of ERBOCo-5 are significantly lower than those of the other two numerically designed alloys, which can mainly be explained by the much higher γ' volume fraction and compressive flow stress at the creep test temperature. However, the creep strength of the three numerically designed alloys is inferior to that of conventionally designed ERBOCo-1, which shows the lowest creep rates and thus the highest creep strength. The reason for the superior mechanical properties of ERBOCo-1 at the test temperature compared to ERBOCo-6 and -7 is most likely its higher γ' volume fraction. The inferior creep strength of ERBOCo-5 compared to ERBOCo-1 could also be explained by the γ' volume fraction. This time, a very high γ' volume fraction of 80 pct in ERBOCo-5 may be disadvantageous in the way that if the number of narrow γ channels is low, the γ' phase becomes the matrix phase. Therefore, the effectiveness of precipitation hardening decreases compared to ERBOCo-1, which has a γ' volume fraction of about 60 pct. The presence of additional detrimental intermetallic phases like the B2 phase in ERBOCo-5 may also deteriorate the creep properties. However, the influence of the B2 phase on the mechanical properties could not be isolated.

IV. DISCUSSION

A. *Database Accuracy*

The entire computational alloy design approach employed in this study requires an accurate description of an alloy's thermodynamic properties to make precise predictions of the thermophysical properties and, finally, the mechanical strength and the application performance. In optimization, it is strictly only necessary to adequately describe the properties' relative values. Thus, it would be acceptable if, *e.g.,* the absolute calculated densities were not accurate, if the relative values match between calculations and reality. A genetic optimization algorithm could still find the compositions with minimal density if this requirement is fulfilled. An accurate representation of reality is much more critical concerning optimization constraints since possible solutions are outright discarded if they violate any constraint.

Trends in transition temperatures are generally well described, even though they are all consistently overestimated by all databases. The accuracy of solidus and liquidus temperatures is adequate, with a deviation of about 20 °C. The prediction for the γ' solvus temperature is less satisfying, with a deviation of about 40 °C. Deviations of equal magnitude between measured and calculated transition temperatures were found in literature for modified commercial Ni-base superalloys (TCNI8/TTNI8 databases)[52] and the SB-CoNi alloy series (PanCobalt database, PANDAT).[35] Similarly, the γ' fractions in dependence on the temperature are described qualitatively well except for ERBOCo-6 and -7 below 800 °C. However, at such a low temperature, diffusion starts to become sluggish, which makes it difficult to obtain reliable data on the equilibrium state. Therefore, some deviations may be expected in this temperature regime.

A different picture arises concerning the elemental partitioning between the γ and γ' phases. The CALPHAD databases very well describe Co, Ni, Al, and Cr partitioning. For Ti, the predictions are less accurate. However, the calculated partitioning of the solid solution strengtheners Mo and W is quite different from the experimental coefficients. W is predicted to be enriched in the γ matrix, just as in Ni-base superalloys. In contrast, the measurements show a nearly even distribution between the precipitate and matrix phase. This inaccuracy could be explained by an improper description of the $Co_3(Al,W)$ phase in the CALPHAD databases. In Co-rich superalloys, W contributes strongly to the stability of the γ' phase, making up a significant part of its composition. If the required amount of W for γ' stabilization were lower in the database description, this would lead to a more substantial partitioning of W to the matrix. However, the general trend in partitioning behavior appears to be reproduced. With the addition of Co, more W is bound in the γ' phase, which ultimately reduces the maximum attainable I_{sss} in Co-rich alloys relative to Ni-base alloys (Figure 1). For Mo, the behavior is reversed: while Mo partitions to the matrix, an equally strong partitioning to the precipitate phase is predicted by CALPHAD. This has severe implications for the actual solid solution hardening. According to the APT measurement, ERBOCo-6 and -7 have an I_{sss} of 11.5 and 12.1, respectively. These values are far higher than the calculated I_{sss} of 8.26 and 9.63 at 900 °C. In principle, a higher I_{sss} is beneficial for alloy strength. However, this significant deviation between prediction and experiment raises the question if better compromises between a high γ' fraction and high solid strengthening could have been achieved with a more accurate database.

Finally, the Scheil solidification simulations could predict the presence or absence of intermetallic phases in the as-cast state. For ERBOCo-5, a fraction of $\gamma/\beta/\mu$ eutectic of ~ 22 pct was calculated. In contrast, the measured area fraction of the B2 phase was just over 8 pct, and the EPMA mappings analysis suggests a fraction of 10–12 pct B2 phase. The Scheil simulation does not directly reveal the final fractions of each phase in the as-cast state. Since both γ and β phases form in parallel according to the simulation, one can reasonably assume a B2 fraction below 22 pct. It should be noted that Scheil simulations are a worst-case scenario in that microsegregation will be maximal, as no composition equilibration by diffusion is considered. The incorporation of back-diffusion may further improve the predictive capabilities of Scheil simulations at the expense of a longer calculation time. Furthermore, back-diffusion also requires reliable mobility data. Given the inaccuracies in the predictions of simple equilibrium calculations revealed in this study, the reliability of mobility data in the considered composition range must be evaluated critically.

Since the databases we used were primarily developed for Ni-base superalloys and are most accurate for compositions close to commercial superalloys, the above inaccuracies are not surprising. Still, further computational development of high-performance Co- or CoNi-base superalloys requires a higher fidelity of the thermodynamic predictions.

B. *Fulfillment of Alloy Design Goals*

The aims of reducing density while maintaining high strength and creep resistance (ERBOCo-5) and achieving a homogeneous as-cast microstructure together with adequate strength (ERBOCo-6/-7) have been mainly fulfilled.

With ERBOCo-5, high flow stress at elevated temperatures could be achieved. Indeed, its compressive flow stress of ~ 550 MPa at 850 °C is the highest among the CoNi-base alloys considered here (Figure 11). Co-W-Al-Ti alloys without Ni could achieve slightly higher flow stresses but at the expense of a much higher density above 9000 kg/m^3.[53] Remarkably, ERBOCo-5 is the only alloy in which the flow stress rises initially with higher temperatures. However, the low-temperature strength was not a consideration in the optimization procedure, as the alloy was designed for application at high-temperature. Integration of low-temperature strength into the computational design procedure would require models with high predictive capabilities that might need to consider γ' particle size and alignment as well as precipitate-dislocation interactions.

The creep resistance of ERBOCo-5 is not quite as high as that of ERBOCo-1, with the minimum creep rate being about three times higher. Nevertheless, the minimum creep rate lies within the regime expected for CoNi-base superalloys of 10^{-7} s^{-1} -10^{-8} s^{-1} at 900 °C and 250 MPa.[50] The density of ERBOCo-5 is the lowest among the three experimental alloys. It is also lower than that of the conventionally developed alloy ERBOCo-1, thereby having the best strength-to-density ratio of the considered alloys regarding yield strength at high temperatures. However, the actual density is higher than the predicted one. Concerning the creep resistance, ERBOCo-1 still has a better ratio to density due to its superior minimum creep rate.

A sufficiently high solidus temperature above 1280 °C could be achieved. The γ' fraction, which was constrained to a range between 43 and 47 pct at 1100 °C, is significantly lower in practice than predicted by CALPHAD. Above 1050 °C, the γ' fraction lies slightly below that of ERBOCo-1, whereas the precipitate fraction rises above the values of ERBOCo-1 and the calculated ones at lower temperatures.

The suppression of potentially detrimental intermetallic phases was unsuccessful, as thermodynamic equilibrium calculations cannot capture the full complexity of non-equilibrium processes such as solidification. As Figure 4 demonstrates, it is possible to reasonably predict the appearance of non-equilibrium phases by Scheil solidification simulations, even if the thermodynamic database exhibits notable errors in transition temperatures or the stability of, *e.g.,* the γ' phase. The effect of the B2 phase on the mechanical properties has not been investigated in detail. Wen *et al*. found cracks forming around the β particles in CoNi-base superalloy with ~ 10 vol pct β phase, which was claimed to relieve grain boundary brittleness.[36] Under dynamic load, however, any β phase that may induce cracks would likely be highly detrimental.

An extremely homogeneous casting structure has been achieved with the development of ERBOCo-6 and -7. Intermetallic phases were only present in minuscule amounts, which a homogenization heat treatment could readily dissolve. While their densities are notably higher than calculated, they are still below the upper limit of 9000 kg/m^3. Due to the low γ' solvus temperatures, which are directly correlated to the low γ' volume fractions of these alloys, the heat treatment window (T_{sol}- $T_{\gamma'}$) is quite broad, so that a homogenization heat treatment and forging can be carried out in a wide temperature range. The low γ' content and the homogeneous microstructure are related: an increased concentration of Al increases microsegregation during solidification, which ultimately causes the formation of the Al-rich B2 phase. In retrospect, the alloy selection was quite strict with regard to the eutectic fraction. B2 and other undesirable phases could probably have been avoided by choosing alloys with a higher predicted eutectic fraction. Standard Scheil solidification tends to overestimate the degree of segregation, since no diffusion in the solid is considered. However, the threshold of calculated eutectic fraction below which no additional phases are observed experimentally is not known initially. Accepting a higher eutectic fraction would have allowed the selection of potentially stronger alloys with a higher γ' content.

The I_{sss} of ERBOCo-7 is the highest of the three alloys, followed closely by ERBOCo-6. As discussed above, significant discrepancies exist between calculations and APT measurements regarding the partitioning of the refractory elements. Due to the reversed partitioning of Mo compared to CALPHAD predictions, the actual I_{sss} values are far higher than the designed ones. The high I_{sss} seems beneficial at low temperatures; at higher temperatures, however, the lack of a sufficient fraction of the γ' phase leads to lowered strength and creep resistance. If element partitioning and γ' phase fractions were described better for Co-rich compositions by the thermodynamic databases, it might be possible to develop alloys that are as homogeneous but stronger and more resistant to creep.

C. *Potential Applications for the Designed Alloys*

The optimized alloys were primarily developed to explore if the design strategy and criteria adequate for developing Ni-base superalloys are still applicable to Co-rich alloys. ERBOCo-5 seems not to have the potential for technical applications due to its low strength at medium to low temperatures and the presence of the B2 phase. However, the very low density shows that there is still room for improving the density of CoNi-base alloys. ERBOCo-6 and -7, on the other

hand, could be interesting materials for various manufacturing processes owing to the extremely high homogeneity already in the as-cast state.

The high homogeneity and the wide temperature range between solidus and γ' solvus temperature are beneficial for hot working.[54] The low chemical segregation requires only a short homogenization heat treatment, which can be carried out at high temperatures since there is little risk of incipient melting. Furthermore, the solidus temperatures are nearly 150 °C higher than IN718 (1255 °C).[55] Further development might be necessary to include grain boundary-pinning precipitates to prevent excessive grain growth during processing.

V. CONCLUSIONS

We have developed three experimental alloys by computational optimization of their properties to investigate the possibility of developing new CoNi-base superalloys using CALPHAD calculations. We draw the following conclusions:

1. CoNi alloys with a high content of γ' phase can be developed based on thermodynamic calculations. Due to their high Al content, they tend to form B2 phase in the interdendritic region, which may be detrimental to creep and fatigue life.
2. Scheil calculations are necessary to predict the formation of the B2 phase computationally. By adjusting the design goals, alloys free of B2 phase can be produced.
3. As a high degree of microsegregation, especially of Al, is a prerequisite for forming B2 phase, alloys optimized for small intermetallic phase fractions have an extremely homogeneous microstructure.
4. CALPHAD predictions are mostly too optimistic in comparison to reality. Transition temperatures and γ' fractions are predicted to be too high. The partitioning behavior is described well except for the solid solution strengtheners Mo and W.
5. Although the alloys were designed only as concept studies, ERBOCo-6 and -7 could be interesting for processing by forging or additive manufacturing due to their highly homogeneous microstructure. Better thermodynamic databases will allow for designing Co-rich alloys with further improved properties.

ACKNOWLEDGMENTS

The authors acknowledge funding by the Deutsche Forschungsgemeinschaft (DFG) through projects B3, C7, and Z01 of the Collaborative Research Center SFB/TR 103: "From Atoms to Turbine Blades—A Scientific Approach for Developing the Next Generation of Single Crystal Alloys." The authors further gratefully acknowledge the support of S. Michel in performing the EPMA measurements and of S. Fiedler and P. Randelzhofer for the DSC measurements.

CONFLICT OF INTEREST

The authors declare that they have no conflict of interest.

FUNDING

Open Access funding enabled and organized by Projekt DEAL.

OPEN ACCESS

REFERENCES

1. C.H. Zenk, S. Neumeier, N.M. Engl, S.G. Fries, O. Dolotko, M. Weiser, S. Virtanen, and M. Göken: *Scr. Mater.*, 2016, vol. 112, pp. 83–86.
2. J. Sato, T. Omori, K. Oikawa, I. Ohnuma, R. Kainuma, and K. Ishida: *Science (80-)*, 2006, vol. 312, pp. 90–91.
3. T. Omori, K. Oikawa, J. Sato, I. Ohnuma, U.R. Kattner, R. Kainuma, and K. Ishida: *Intermetallics*, 2013, vol. 32, pp. 274–83.
4. I. Povstugar, P.P. Choi, S. Neumeier, A. Bauer, C.H. Zenk, M. Göken, and D. Raabe: *Acta Mater.*, 2014, vol. 78, pp. 78–85.
5. N. Volz, C.H. Zenk, R. Cherukuri, T. Kalfhaus, M. Weiser, S.K. Makineni, C. Betzing, M. Lenz, B. Gault, S.G. Fries, J. Schreuer, R. Vaßen, S. Virtanen, D. Raabe, E. Spiecker, S. Neumeier, and M. Göken: *Metall. Mater. Trans. A*, 2018, vol. 49A, pp. 4099–4109.
6. J. Koßmann, C.H. Zenk, I. Lopez-Galilea, S. Neumeier, A. Kostka, S. Huth, W. Theisen, M. Göken, R. Drautz, and T. Hammerschmidt: *J. Mater. Sci.*, 2015, vol. 50, pp. 6329–38.
7. N. Volz, F. Xue, A. Bezold, C.H. Zenk, S.G. Fries, J. Schreuer, S. Neumeier, and M. Göken: *Metall. Mater. Trans. A*, 2021, vol. 52A, pp. 3931–44.
8. J. Ruan, W. Xu, T. Yang, J. Yu, S. Yang, J. Luan, T. Omori, C. Wang, R. Kainuma, K. Ishida, C.T. Liu, and X. Liu: *Acta Mater.*, 2020, vol. 186, pp. 425–33.

9. M. Montakhab and E. Balikci: *Metall. Mater. Trans. A*, 2019, vol. 50A, pp. 3330–42.
10. B.D. Conduit, N.G. Jones, H.J. Stone, and G.J. Conduit: *Mater. Des.*, 2017, vol. 131, pp. 358–65.
11. R.C. Reed, T. Tao, and N. Warnken: *Acta Mater.*, 2009, vol. 57, pp. 5898–5913.
12. L. Zhang, Z. Huang, Y. Pan, and L. Jiang: *Model. Simul. Mater. Sci. Eng.*, 2019, vol. 27, p. 065002.
13. Z. Qin, Z. Wang, Y. Wang, L. Zhang, W. Li, J. Liu, Z. Wang, Z. Li, J. Pan, L. Zhao, F. Liu, L. Tan, J. Wang, H. Han, L. Jiang, and Y. Liu: *Mater. Res. Lett.*, 2021, vol. 9, pp. 32–40.
14. P. Liu, H. Huang, S. Antonov, C. Wen, D. Xue, H. Chen, L. Li, Q. Feng, T. Omori, and Y. Su: *npj Comput. Mater.*, 2020, vol. 6, pp. 1–9.
15. Y.T. Tang, C. Panwisawas, J.N. Ghoussoub, Y. Gong, J.W.G. Clark, A.A.N. Németh, D.G. McCartney, and R.C. Reed: *Acta Mater.*, 2021, vol. 202, pp. 417–36.
16. E. Menou, G. Ramstein, E. Bertrand, and F. Tancret: *Model. Simul. Mater. Sci. Eng.*, 2016, vol. 24, p. 055001.
17. R. Rettig, N.C. Ritter, H.E. Helmer, S. Neumeier, and R.F. Singer: *Model. Simul. Mater. Sci. Eng.*, 2015, vol. 23, p. 035004.
18. A. Müller, M. Sprenger, N.C. Ritter, R. Rettig, M. Markl, C. Körner, and R.F. Singer: *Model. Simul. Mater. Sci. Eng.*, 2019, vol. 27, p. 025001.
19. A. Müller, I. Roslyakova, M. Sprenger, P. Git, R. Rettig, M. Markl, C. Körner, and R.F. Singer: *Model. Simul. Mater. Sci. Eng.*, 2019, vol. 27, p. 024001.
20. M. Markl, A. Müller, N. Ritter, M. Hofmeister, D. Naujoks, H. Schaar, K. Abrahams, J. Frenzel, A.P.A. Subramanyam, A. Ludwig, J. Pfetzing-Micklich, T. Hammerschmidt, R. Drautz, I. Steinbach, R. Rettig, R.F. Singer, and C. Körner: *Metall. Mater. Trans. A*, 2018, vol. 49A, pp. 4134–45.
21. R. Rettig, K. Matuszewski, A. Müller, H.E. Helmer, N.C. Ritter, and R.F. Singer: *Proc. Int. Symp. Superalloys*, 2016, pp. 35–44.
22. B. Wahlmann, D. Leidel, M. Markl, and C. Körner: *Crystals*, 2021, vol. 11, p. 902.
23. S. Neumeier, L.P. Freund, and M. Göken: *Scr. Mater.*, 2015, vol. 109, pp. 104–07.
24. P. Caron: in *Superalloys 2000 (Ninth International Symposium)*, vol. 132, TMS, 2000, pp. 737–46.
25. E. Fleischmann, M.K. Miller, E. Affeldt, and U. Glatzel: *Acta Mater.*, 2015, vol. 87, pp. 350–56.
26. O.M. Horst, D. Schmitz, J. Schreuer, P. Git, H. Wang, C. Körner, and G. Eggeler: *J. Mater. Sci.*, 2021, vol. 56, pp. 7637–58.
27. A.B. Kamara, A.J. Ardell, and C.N.J. Wagner: *Metall. Mater. Trans. A*, 1996, vol. 27A, pp. 2888–96.
28. R.N. Abdullaev, R.A. Khairulin, Y.M. Kozlovskii, and S.V. Stankus: *Metall. Mater. Trans. A*, 2021, vol. 52A, pp. 5449–56.
29. J. Zhang and P.A. Korzhavyi: *Metals*, 2020, vol. 10, p. 319.
30. Q. Yao, S.-L. Shang, Y.-J. Hu, Y. Wang, Y. Wang, Y.-H. Zhu, and Z.-K. Liu: *Intermetallics*, 2016, vol. 78, pp. 1–7.
31. Q. Yao, S.-L. Shang, K. Wang, F. Liu, Y. Wang, Q. Wang, T. Lu, and Z.-K. Liu: *J. Mater. Res.*, 2017, vol. 32, pp. 2100–08.
32. K. Deb, A. Pratap, S. Agarwal, and T. Meyarivan: *IEEE Trans. Evol. Comput.*, 2002, vol. 6, pp. 182–97.
33. J. Blank and K. Deb: *IEEE Access*, 2020, vol. 8, pp. 89497–89509.
34. M.V. Nathal: *Metall. Trans. A*, 1987, vol. 18, pp. 1961–70.
35. C.A. Stewart, S.P. Murray, A. Suzuki, T.M. Pollock, and C.G. Levi: *Mater. Des.*, 2020, vol. 189, p. 108445.
36. M. Wen, Y. Sun, J. Yu, Y. Yang, and Y. Zhou: *J. Alloys Compd.*, 2020, vol. 835, 155337.
37. Y. Xu, L. Zhang, J. Li, X. Xiao, X. Cao, G. Jia, and Z. Shen: *Mater. Sci. Eng. A*, 2012, vol. 544, pp. 48–53.
38. S. Giese, A. Bezold, M. Pröbstle, A. Heckl, S. Neumeier, and M. Göken: *Metall. Mater. Trans. A*, 2020, vol. 51A, pp. 6195–6206.
39. M. Ganesan, D. Dye, and P.D. Lee: *Metall. Mater. Trans. A*, 2005, vol. 36A, pp. 2191–2204.
40. E. Scheil: *Z. Metallk.*, 1942, vol. 34, pp. 70–72.
41. K. Thompson, D. Lawrence, D.J. Larson, J.D. Olson, T.F. Kelly, and B. Gorman: *Ultramicroscopy*, 2007, vol. 107, pp. 131–39.
42. M.K. Miller, K.F. Russell, K. Thompson, R. Alvis, and D.J. Larson: *Microsc. Microanal.*, 2007, vol. 13, pp. 428–36.
43. M. Lenz, Y.M. Eggeler, J. Müller, C.H. Zenk, N. Volz, P. Wollgramm, G. Eggeler, S. Neumeier, M. Göken, and E. Spiecker: *Acta Mater.*, 2019, vol. 166, pp. 597–610.
44. C.H. Zenk, N. Volz, C. Zenk, P.J. Felfer, and S. Neumeier: *Crystals*, 2020, vol. 10, p. 1058.
45. L. Rachmawati and D. Srinivasan: *IEEE Trans. Evol. Comput.*, 2009, vol. 13, pp. 810–24.
46. E.A. Lass, D.J. Sauza, D.C. Dunand, and D.N. Seidman: *Acta Mater.*, 2018, vol. 147, pp. 284–95.
47. W. Hermann, M. Fahrmann, and H.G. Sockel: *Proc. Int. Symp. Superalloys*, 2004, pp. 517–22.
48. H. Chandler: *Heat Treater's Guide: Practices and Procedures for Nonferrous Alloys*, Materials Park, OH, ASM International, 2006, pp. 63–67.
49. C.M.F. Rae, M.S.A. Karunaratne, C.J. Small, R.W. Broomfield, C.N. Jones, and R.C. Reed: 2012, pp. 767–76.
50. C.H. Zenk, S. Neumeier, M. Kolb, N. Volz, S.G. Fries, O. Dolotko, I. Povstugar, D. Raabe, and M. Göken: *Proc. Int. Symp. Superalloys*, 2016, pp. 971–80.
51. S. Meher, M.C. Carroll, T.M. Pollock, and L.J. Carroll: *Mater. Des.*, 2018, vol. 140, pp. 249–56.
52. K. Ventura, D. Beaudry, A. Aviles, A. Kapustina, P. Draa, K. Patel, R. Snider, and G. Fuchs: *Proc. Int. Symp. Superalloys,* 2020, pp. 103–11.
53. C.H. Zenk, S. Neumeier, H.J. Stone, and M. Göken: *Intermetallics*, 2014, vol. 55, pp. 28–39.
54. J.W. Brooks: *Mater. Des.*, 2000, vol. 21, pp. 297–303.
55. H. Hosaeus, A. Seifter, E. Kaschnitz, and G. Pottlacher: *High Temp. Press.*, 2001, vol. 33, pp. 405–10.